Physics and Imaging in Radiation Oncology 28 (2023) 100517

Contents lists available at ScienceDirect

Physics and Imaging in Radiation Oncology

journal homepage: www.sciencedirect.com/journal/physics-and-imaging-in-radiation-oncology

Original Research Article

Multi-camera optical tracking and fringe pattern analysis for eye surface profilometry in ocular proton therapy

Riccardo Via [a,*], Katarina Bryjova [a], Alessia Pica [a], Guido Baroni [b], Antony Lomax [a], Damien Charles Weber [a,c,d], Giovanni Fattori [a], Jan Hrbacek [a]

[a] Center for Proton Therapy, Paul Scherrer Institute, CH-5232 Villigen, Switzerland
[b] Dipartimento di Elettronica Informazione e Bioingegneria, Politecnico di Milano, Milano 20133, Italy
[c] Department of Radiation Oncology, University Hospital of Zürich, Switzerland
[d] Department of Radiation Oncology, Inselspital, Bern University Hospital, University of Bern, Switzerland

ARTICLE INFO

Keywords:
Ocular Proton Therapy
IGRT
Optical tracking
Eye Tracking
Fringe Pattern Profilometry

ABSTRACT

Background and purpose: An optical tracking system for high-precision measurement of eye position and orientation during proton irradiation of intraocular tumors was designed. The system performed three-dimensional (3D) topography of the anterior eye segment using fringe pattern analysis based on Fourier Transform Method (FTM).

Materials and methods: The system consisted of four optical cameras and two projectors. The design and modifications to the FTM pipeline were optimized for the realization of a reliable measurement system. Of note, phase-to-physical coordinate mapping was achieved through the combination of stereo triangulation and fringe pattern analysis. A comprehensive pre-clinical validation was carried out. Then, the system was set to acquire the eye surface of patients undergoing proton therapy. Topographies of the eye were compared to manual contouring on MRI.

Results: Pre-clinical results demonstrated that 3D topography could achieve sub-millimetric accuracy (median:0.58 mm) and precision (RMSE:0.61 mm) in the clinical setup. The absolute median discrepancy between MRI and FTM-based anterior eye segment surface reconstruction was 0.43 mm (IQR:0.65 mm)

Conclusions: The system complied with the requirement of precision and accuracy for image guidance in ocular proton therapy radiation and is expected to be clinically tested soon to evaluate its performance against the current standard.

1. Introduction

Conventional eye tracking techniques, when applied for eye localization in ocular proton therapy, have shown shortcomings exhibiting either low accuracy or insufficient reliability [1]. This failure is due to methodological and practical reasons: firstly, conventional eye-tracking techniques do not aim for complete six-degree-of-freedom eye localization, but rather provide an estimate of the subject's fixation point, often as a result of a specific calibration procedure involving significant anatomical simplifications [2]; secondly, video-oculography relies on the detection of sharp corneal reflections originating from light sources, a condition difficult to realize in clinical settings characterized by the dryness of the eye due to the use of eyelid retractors, a prerequisite for proton irradiation [3]. Due to these difficulties, unconventional eye tracking solutions have been here investigated. Fringe pattern analysis for surface measurement, based on Fourier Transform Methods (FTM), is not unprecedented in either ophthalmology or radiation therapy, but has mostly been dedicated to accurate corneal-scleral topography for diagnostic or scleral lens fitting or thoracic surface measurements [4–8].

FTM, proposed by Takeda et al in the 1980s [9,10] is a method for non-contact 3D surface reconstruction inferred from the deformation of a Ronchi pattern imaged with an optical camera. Three-dimensional topography then involves: imaging of the deformation of a fringe pattern on an object of interest (i); demodulation with a spatial carrier frequency for phase retrieval (ii) [9–11]; phase unwrapping (iii) [12–17]; phase-to-height mapping and transversal scaling (iv) [8,18–20]. In the last four decades, methodologies for solving each one of these steps have been the subject of extensive study for use in a

* Corresponding author at: WMSA/C29, 5232 Villigen PSI, Switzerland.
E-mail address: riccardo.via@psi.ch (R. Via).

https://doi.org/10.1016/j.phro.2023.100517
Received 15 August 2023; Received in revised form 13 November 2023; Accepted 13 November 2023
Available online 20 November 2023

number of different applications [8,21]. In particular, the reliability and accuracy of translating a phase map into a measurement in 3D space (iv) is of critical importance in the context of patient localization systems in high-precision radiotherapy. As such, our study proposes alternative calibration procedures and methodological solutions to achieve high-precision measurements by combining stereo triangulation and fringe profilometry.

This study focused on the use of FTM as a tool for corneal-scleral topography in the context of radiotherapy treatments of intraocular tumors [22]. An accurate and precise three-dimensional surface reconstruction of the anterior eye segment could be used to verify the patient position before irradiation, a task that is currently carried out using radiographic imaging of surgically implanted clips. FTM has the potential to achieve this without exposing the patient to noncurative dose and has the advantage, compared to feature-based or triangulation-based conventional eye tracking techniques, of being more robust and efficient. The systems performance was evaluated in a pre-clinical study using geometric phantoms following the principles for quality assurance of localization systems in medical applications, with specific reference to image guided radiation therapy. Subsequently, its capability of correctly reconstructing the eye surface was evaluated in a prospective clinical study.

2. Materials and methods

2.1. System description

The system proposed here consisted of four optical cameras and two fringe pattern projectors divided into two distinct optical 'units', each composed of two sensors and one projector (see Fig. 1). Two 3 W infrared (peak wavelength: 850 nm) LED projectors (LTPRHP3W-8, OptoEngineering srl, Mantova, Italy) were positioned to project a vertical Ronchi grating of 5 lines/cm onto the eye surface. Deformation of this pattern was then recorded by 4 cameras with good sensitivity in the near-infrared spectrum (UI-5240LE-NIR-GL-MB, IDS Imaging Development System, Obersulm, Germany) with resolutions of 640x512 pixels (after horizontal and vertical binning to a pixel size of 10.6 μm) and frame rates of 25 Hz. All optical elements were equipped with 25 mm focal length lenses (SV-2514H, VS Technology, Japan, Tokyo).

To ensure that all measurements by the optical units were geometrically consistent, a world coordinate system (WCS) was defined (see Fig. 1). Projectors were oriented at 45-degrees to the Z axis and were roughly aligned to the X-Z plane, with the two coupled optical sensors being arranged symmetrically below and above this plane (see Fig. 1). The two optical units, i.e. the bundle of two cameras and one projector, pointed to the origin of the WCS from a distance of 20 cm and 25 cm for the projectors and the sensors respectively. This configuration, with one optical unit facing the patient on the right and the other the left, was specifically designed to ensure a line of sight to the eye surface by at least one of the two units, regardless of whether the patient's right or left eye was being treated.

As previously mentioned, the system was intended for use during proton therapy of intraocular tumors. In these treatments, a horizontal fixed proton beamline is used so it is the position of the target, i.e. the intraocular tumor, that needs to be adjusted to guarantee that it is covered by the proton beam. The measurement of the anterior eye segment performed by the proposed system could be used to verify the patient position, a task that in the current clinical workflow is performed using iterative X-ray imaging. System performance validation was specifically designed to assess the capability of the system in the context of its application. Firstly, to ensure that the proposed system measurements were relevant for this application, the arrangement of the WCS replicated the isocentric reference frame defined for IGRT in ocular proton therapy with the Z-axis aligned to the proton beam and pointing to the source, the Y axis oriented vertically and the axis X pointing from right to left.

2.2. Three-dimensional surface reconstruction

Fringe pattern analysis of the distorted Ronchi grating was based on the Fourier Transform Method for fringe demodulation introduced by Takeda in [9,10]. The theory of FTM, along with the modifications applied for this work, are briefly described in the supplementary material. Here, the focus was on the two-step method for translating the measured relative unwrapped phase $\Delta\varnothing(i,j)$, the result of the FTM pipeline, into a 3D topography of a surface. Firstly, a phase-to-height calibration procedure to define the necessary, camera specific coefficients translating phase to height (the out-of-plane coordinate-Z) is presented. Then, the method to determine the transversal position (X,Y), based on the stereo calibration parameters of the sensors, is described.

The system was calibrated for surface reconstruction using a dedicated procedure to translate the unwrapped phase map into an out-of-plane measurement in the WCS. During this process, the system was set to acquire a series of images of a circular flat surface at different known positions along the Z-axis (1 mm step from −10 mm to +25 mm with respect to the origin of WCS). Then a large rectangular planar surface, whose dimension covers the entire field-of-view of the optical sensors, was imaged once (with Z equals to +10 mm) as the reference plane of acquisition (see Fig. 2(a)).

The phase-to-height mapping algorithm then followed the implementation introduced by Du and Wang [19], which relies on the calculation of 11 parameters ($c_{1,2,..5}$,$d_{0,1,..5}$) for each optical sensor.

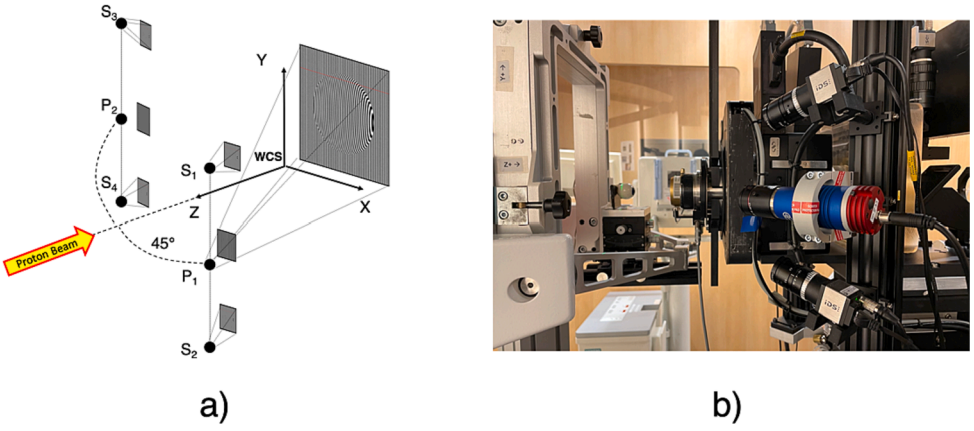

Fig. 1. A schematic representation of the system is presented in panel (a). The projector P_1 illuminates the scene with a Ronchi pattern. The deformation of this pattern is visible on the images acquires by two sensors S_1 and S_2. The other system's unit (P_2, S_3 and S_4) is mirrored on the opposite side of the Z axis. In panel (b) our actual setup is shown. The right-hand side optical unit (P_2, S_3 and S_4) is visible.

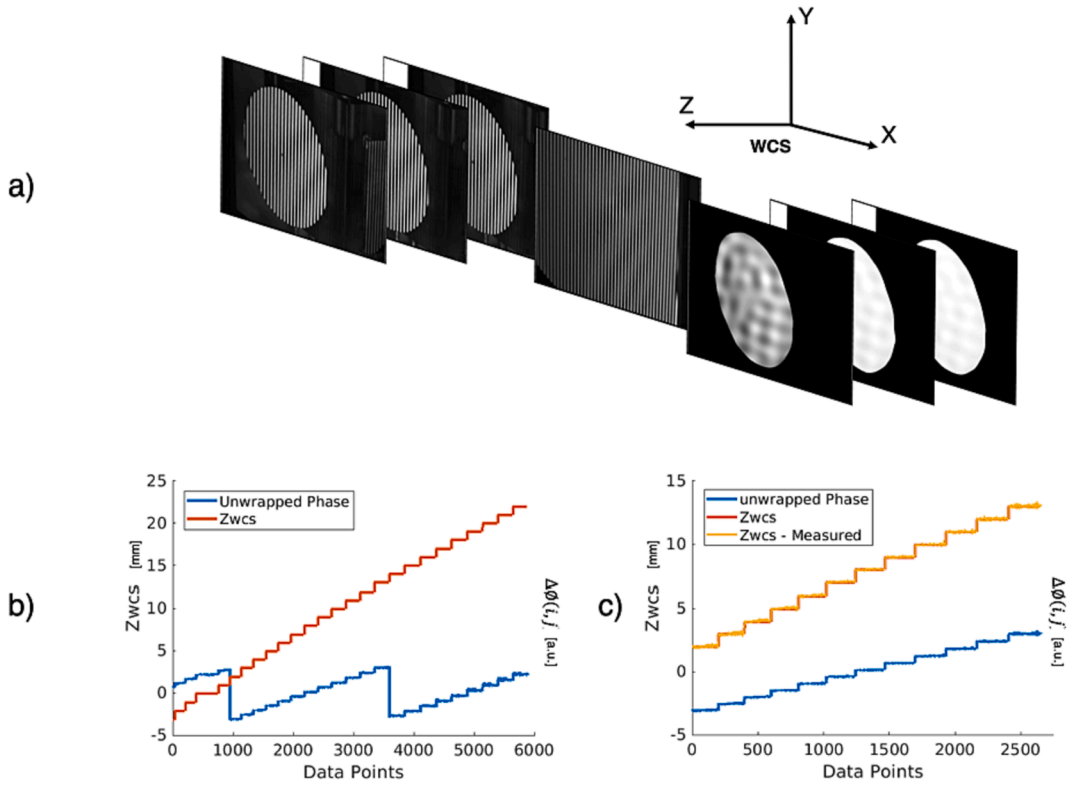

Fig. 2. Panel (a) depicts a schematic representation of the phase-to-height mapping calibration procedures. The sensors acquire images of the fringe pattern projection on a planar circular object at different, but known out-of-plane positions. The calibration object is moved by 1 mm steps. A reference image is also acquired using a larger planar object at a fixed position. By applying FTM, the calculated unwrapped phase, in relation with the out-of-plan position, along the Z axis of the world coordinate system can be seen on panel (b). The non-monotonic trend of the unwrapped phase is due to the intrinsic periodicity of the quasi-sinusoidal fringe pattern used. To estimate the parameters of the governing equation [19] mapping phase to height, the largest monotone portion of the function is selected (panel c). This does not compromise the surface reconstruction in the volume of interest and, at the same time, limits the number of parameters for the sensor to eleven.

$$Z = \frac{1 + c_1 \bullet \Delta\varnothing(i,j) + (c_2 + c_3 \bullet \Delta\varnothing(i,j)) \bullet i + (c_4 + c_5 \bullet \Delta\varnothing(i,j)) \bullet j}{d_0 + d_1 \bullet \Delta\varnothing(i,j) + (d_2 + d_3 \bullet \Delta\varnothing(i,j)) \bullet i + (d_4 + d_5 \bullet \Delta\varnothing(i,j)) \bullet j}$$

These eleven coefficients were determined using the Levenberg-Marquardt algorithm with the least-squares error S defined as:

$$S = \sum_{i=1}^{M} \left[\frac{1 + c_1 \bullet \Delta\varnothing(i,j) + (c_2 + c_3 \bullet \Delta\varnothing(i,j)) \bullet i + (c_4 + c_5 \bullet \Delta\varnothing(i,j)) \bullet j}{d_0 + d_1 \bullet \Delta\varnothing(i,j) + (d_2 + d_3 \bullet \Delta\varnothing(i,j)) \bullet i + (d_4 + d_5 \bullet \Delta\varnothing(i,j)) \bullet j} - Z_i \right]^2$$

Fig. 2(b) shows the measured relative unwrapped phase $\Delta\varnothing(i,j)$ for twelve thousand data points acquired with one of the cameras of the system. The use of a quasi-sinusoidal pattern for fringe projection resulted in a periodicity in the unwrapped phase values as a function of out-of-plane positions of the calibration object. Only values comprising the largest monotonic portion of the relative unwrapped phase and their corresponding nominal out-of-plane position were used for the optimization. As a result, only a portion of the field of view was used to estimate the coefficients, being on average between 0 and +15 mm along the Z axis for the four sensors. Fig. 2(c) shows an example of the extracted Z-coordinate against the nominal value using phase-to-height mapping.

To enable 3D measurements in the WCS, the four cameras of the system were modelled as pinhole cameras. Each camera was defined by a 3x4 homogenous camera projection Matrix P = [R|T] with R and T defining the rotation and translation that related the camera coordinate frame to the world coordinate frame [23]. From simultaneous acquisition of images by all sensors of a planar chessboard located at the origin of the WCS, the projection matrix P of each camera was computed, allowing for 3D measurements of points in the WCS.

The 3x4 matrix P that defined the geometry of each sensor could be used to determine the position, in the WCS, of the projection centre C of the camera model and, in turn, of the vector connecting C to a specific 3D point in space M as seen by the camera sensor (m).

$$P = [R|T];$$

$$C = -R^{-1} \bullet T;$$

$$\overrightarrow{CmM}_{WCS} = R^{-1} \bullet \frac{m_c}{\|m_c\|} \overline{CM} = \frac{\overline{C\,C_P}}{\cos(\alpha)}$$

The out-of-plane height of this point, i.e. the Z in WCS, was measured using FTM. By applying basic trigonometry, the X and Y coordinate of point M could then be determined in physical coordinates as M_{WCS}. A schematic representation of this methodology is shown in Fig. 3.

$$\cos(\alpha) = \frac{\overrightarrow{CmM}_{WCS} \bullet [0,0,-1]}{\|\overrightarrow{CmM}_{WCS}\| \bullet \|[0,0,-1]\|}; M_{WCS} = C + \overline{CM} \bullet \overrightarrow{CmM}_{WCS}$$

Thus, every camera providing a useable measurement of relative unwrapped phase $\Delta\varnothing(i,j)$ was capable of estimating the 3D location of the corresponding point in physical coordinates.

2.3. Experimental validation

System accuracy and precision were evaluated using four objects: two 3D printed geometrical objects, a triangular wedge and a circular-based pyramid, and two eye phantoms (see Fig. 4). The system accuracy was then evaluated on fiducial points marked on the surface of the objects. Their 3D location in physical coordinates, estimated through fringe pattern analysis and through triangulation, were compared. Three hundred and seventeen measurements of fiducial point positions, distributed along 16 separate acquisition sessions, were used. Also, the

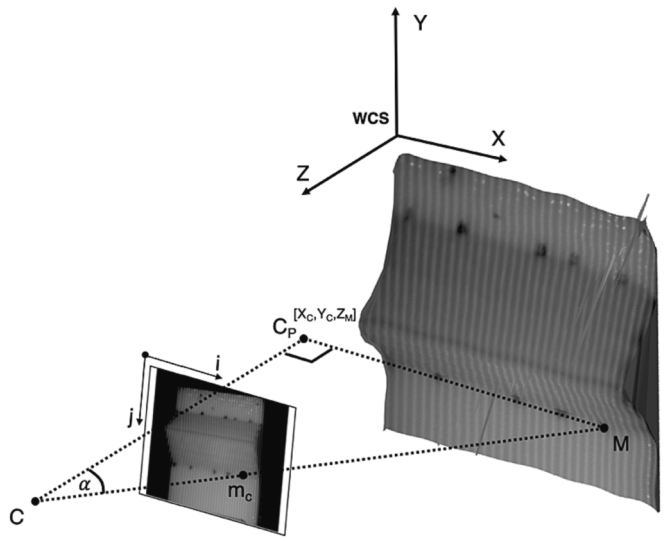

Fig. 3. Schematic representation of the transversal scaling procedure used for the estimation of the X and Y coordinate of points, by a single camera, whose height (Z coordinate) is calculated through FTM and Phase-to-Height mapping. Any point on the image sensor m_c for which an estimate of the relative unwrapped phase and out-of-plane position is available, can be fully reconstructed in physical coordinates by exploiting the sensor stereo calibration parameter and simple trigonometry.

distribution of this discrepancy within the calibration volume was evaluated. Then, to assess the precision of the proposed system, the obtained 3D topographies were compared to a precise characterization of the shape of all four objects obtained using a laser tracker system (Leica AT901 LR, Leica Camera AG, Wetzlar, Germany) providing sub-millimetric precision. The Iterative Closest Point (ICP) algorithm [24] was used to calculate root-mean-square errors (RMSE) of nearest points of the two surfaces after rigid registration. This was followed by a more in-depth analysis on the precision of surface reconstruction for one of the eye phantoms carried out to evaluate the error distribution within the eye surface and the combination of measurements from multiple sensors.

Finally, a preliminary evaluation of the systems clinical capabilities was carried out on sixteen patients undergoing ocular proton therapy within the frame of the EKNZ 2019-01987 project approved by the ethics committee Ethikkommission Nordwest- und Zentralschweiz. Pre-treatment MRI acquisitions of patients (for information on the used sequences please refer to [25]), were contoured to create a personalized eye model that included a definition of the best fitting ellipsoid to the anterior eye segment surface. The system was then set to acquire, concurrently with radiographic imaging of clips during position verification, the eye surface of these patients using one optical unit at a time. This was compared to the absolute position of the anterior eye segment retrieved by aligning the MRI-based geometrical model to the measured clips configuration [22]. As a result, we could quantify the anatomical inaccuracies that affected the optical system as the median absolute distance between all points of the eye topography and the MRI model description of the eye surface.

3. Results

3.1. Optical sensors' calibration

A median reprojection error, i.e. the image distance between a projected point and a measured one, of 0.88 pixel (IQR: 1.44) was measured. As regards phase to height mapping, the median discrepancy between the estimated out-of-plane position and the nominal position was 0.12 mm (IQR: 0.15 mm).

3.2. Accuracy and precision

A median 3D discrepancy between fringe pattern analysis and phase-to-height mapping against triangulation of 0.58 mm (IQR:0.70 mm) was measured. The error distribution within the calibration volume is shown in Fig. 5(a). No significant correlation between the magnitude of errors and the location within the volume was found.

The RMSE after registration using ICP between 3D topographies and laser tracker measurements was evaluated on a total of 42 measurements and a median RMSE of 0.61 mm (IQR: 0.22 mm) and 0.59 mm (IQR:0.10 mm) was measured when both optical units were considered at the same time, i.e. four views, or when one optical unit only was used, i.e. two views, respectively.

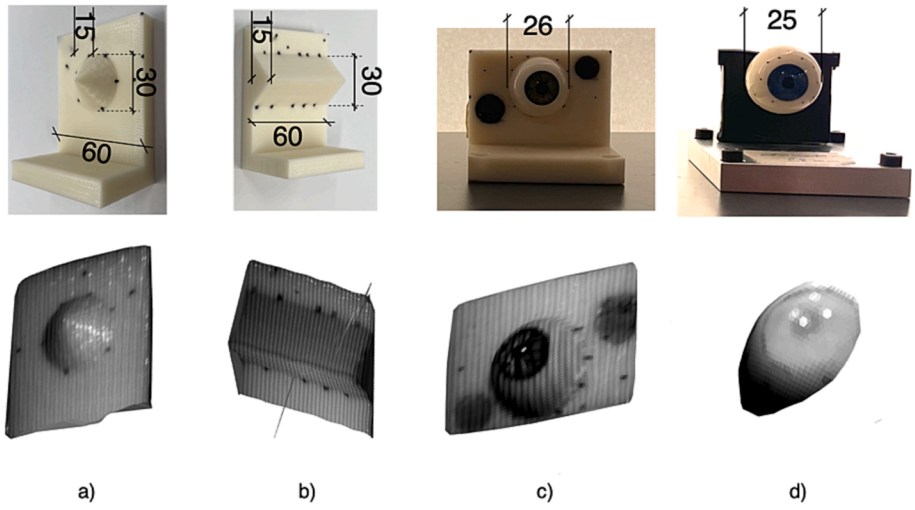

Fig. 4. A picture of the four phantoms used for system validation is presented in the upper panel including the relevant dimensions in mm. A pyramid with a circular base (a), a triangular wedge (b), manufactured with ABS using a Fused Deposition Modelling printer (3D Printer Dimension Elite, Stratasys, US) with a layer thickness of 0.1 mm. The pair of plastic eye phantoms, with irises painted in green and blue are shown respectively (c) and (d) respectively. In the lower panel, an exemplary 3D rendering of a surface reconstruction using FTM is shown for each phantom. Of note, the visibility of the fiducial points, marked on each phantom, is used for accuracy evaluation through comparison with stereo triangulation. (For interpretation of the references to colour in this figure legend, the reader is referred to the web version of this article.)

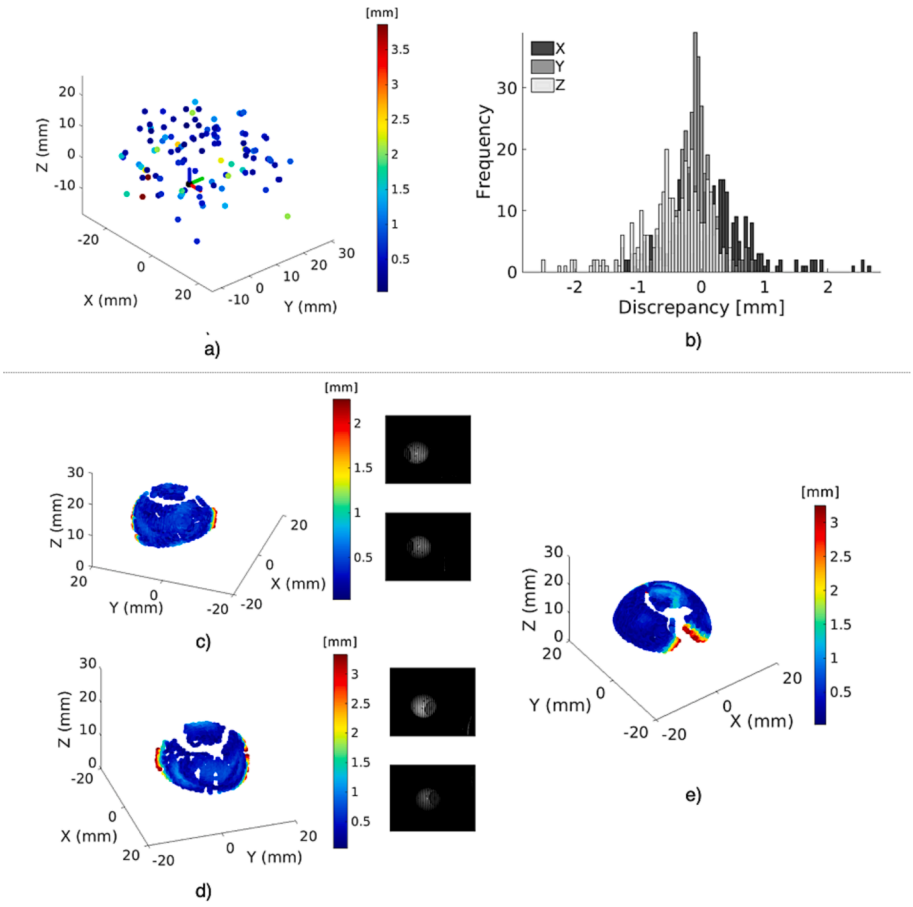

Fig. 5. On panel (a) the accuracy of the system in the calibrated volume is depicted. Panel (b) shows the error distribution in the three directions of the WCS evaluated from fiducials. Panel (c,d and e) show the spatial distribution of the registration error using ICP in the eye phantom. The results are shown separately for the two optical units, each a combination of two sensors and one projector, along with the fringe pattern images acquired by the corresponding sensors in panel (c) and (d). Panel (e) shows the error distribution for the entire eye phantom when combining all measurements of the system.

As seen in Fig. 5(c,d,e), higher errors were measured at the edges of the reconstruction, where the fringe pattern is less visible and the phase map exhibits low spectral power. Within the visible surface of the eye phantom and at the interface of the measurement by the two sensors the error was below 0.6 mm and homogenously distributed. When combining the measurement from the two optical units, a higher error (in the range of 1.0 to 1.5 mm) was visible in the intersection region (Fig. 5 (e)).

Ninety-five separate topographies of the eye, distributed amongst sixteen patients, were directly compared to the MRI-based ellipsoidal model of the anterior eye segment (Fig. 6 (a-b)), resulting in absolute median discrepancies of 0.43 mm (IQR: 9.65 mm). Fig. 6(c) shows the discrepancy distribution for the entire dataset.

4. Discussion

A multi-component optical system, combining stereo triangulation and three-dimensional topography has been presented in this study. The use of FTM for fringe pattern analysis and governing equations for phase-to-height mapping allowed for a static installation of the system

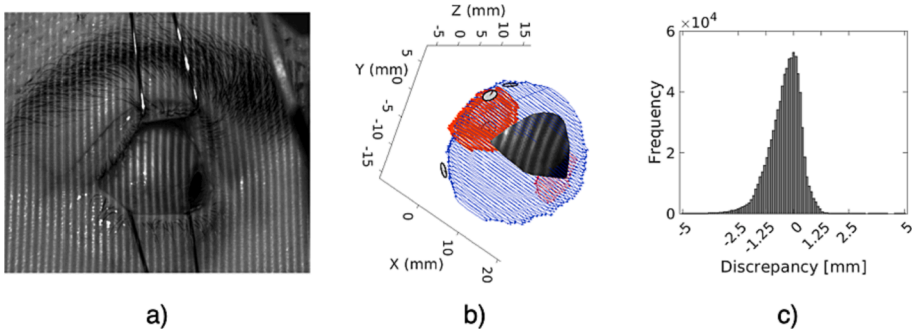

Fig. 6. On panel (a), the fringe pattern projected upon the surface of a patient's eye is visible on the images acquired by two cameras belonging to the same optical unit. The pipeline for 3D topography is applied leading to a 3D reconstruction of the patient's surface and filtered to extract the relevant information for the scleral surface (panel b), On panel (c), the histogram of the distance between the eye topographies extracted from the optical system and the MRI-based ellipsoidal definition of the anterior eye segment is shown.

without any a priori assumption of their arrangement in space. Using four optical cameras, the system provided four geometrically consistent surface reconstructions from multiple vantage points that can be used together or individually. In the context of the system application for corneal topography in therapeutic settings, the setup with the two optical units installed in front of the patient on the right and left guaranteed non-occluded line-of-sight by at least one of the two units regardless of which eye is under examination.

While the conventional FTM method [9] performs under ideal conditions, in real-world conditions, under which the proposed system operates, slight modifications were necessary. In contrast to Price et al [8], who opted for a dynamically adapted filter in the demodulation process, a filter of constant size, centered at a fixed carrier frequency has been designed and applied invariably in the demodulation process. The possibility of adopting such a simpler approach is probably due to the superior quality of the pattern projection obtained with our configuration and components. The LTPRHP3W-8 projector is in fact a single LED coupled with a physical laser-engraved projection pattern and was therefore less susceptible to distortions than conventional active projectors [20]. On the other hand, it was restricted to phase recovery based on a single fringe, making it more difficult to clearly separate the carrier frequency from the background [26]. This design choice reduced the level of precision achieved by this system, which is relatively low if compared to more advanced phase-shifting methods [5,27]. At the same time, however, it was considered favorable for imaging the eye, an object in constant motion, for which maximum instantaneity in data acquisition was required, if at the cost of compromised accuracy [28].

In addition, we have developed a method for phase-to-WCS mapping where the system exploited its capabilities as a multi-camera optical sensor and fringe pattern profilometer. Every sensor was calibrated with respect to the world coordinate system using conventional stereo photogrammetry calibration techniques [22,23] and, in combination with a pixel-based estimation of the out-of-plane position of image features, the translation from phase to height to physical coordinates was efficiently achieved. Also, compared to other approaches for calibration of fringe pattern systems, it did not require a dedicated calibration procedure for the projector or for transversal scaling [8,20]. Compared to Price et al. [8], this implementation limited the number of sensor parameters used for 3D topography to those belonging to the governing equation.

In addition to the procedural advantages and the simplification of the calibration method, the validation results showed that the proposed system can achieve sub-millimetric accuracy in the measurement of fiducial points in WCS coordinates. This result attested to the quality of the cross-calibration between the two optical units. Furthermore, results showed the system's ability to provide 3D topography of objects of comparable precision to a Leica Laser Tracker with a maximum permissible error in the order of tenths of micrometers.

Results exhibited that bundling surface reconstructions from two sensors belonging to the same optical unit did not hinder the precision of the reconstruction, in contrast to what happens when merging information from sensors located at opposite sides. However, this is an eventuality that will not happen during clinical use of the device.

The preliminary results of the clinical study have demonstrated the systems capability to reconstruct 3D topographies of the eye that corresponded well, on average, to the patient's anatomy derived through MRI despite the absence of the fringe model signal in the pupil region. Future activities will focus on the enhancement of the fringe pattern signal by applying fluorescein on the patient's eye [5]. Ultimately, a direct comparison of the optical systems capabilities for accurate patient positioning against the current clinical standard will be carried out. In addition, 3D eye topographies could prove useful to derive realistic models of the patient surface for treatment planning purposes.

Finally, all the designed calibration procedures have been easily accomplished with the existing equipment in the treatment room and could be integrated swiftly in a clinical workflow where time efficiency and ease of use are of the essence.

In conclusion, validation activities showed the robustness of the method under real-world experimental conditions and confirmed the validity of the design for use in eye localization for ocular proton therapy. Provided these positive results are confirmed by a more extended clinical study, X-ray imaging for patient position verification could potentially be replaced by such an optical system combining fringe profilometry and stereo photogrammetry for 3D scleral-corneal topography.

CRediT authorship contribution statement

Riccardo Via: Conceptualization, Data curation, Formal analysis, Investigation, Methodology, Formal analysis, Writing – original draft. **Katarina Bryjova:** Data curation, Methodology. **Alessia Pica:** Data curation, Methodology. **Guido Baroni:** Supervision, Writing – review & editing. **Antony Lomax:** Supervision, Writing – review & editing. **Damien Charles Weber:** Writing – review & editing. **Giovanni Fattori:** Methodology, Investigation, Supervision, Writing – review & editing. **Jan Hrbacek:** Supervision, Funding acquisition.

Declaration of Competing Interest

The authors declare that they have no known competing financial interests or personal relationships that could have appeared to influence the work reported in this paper.

Appendix A. Supplementary data

Supplementary data to this article can be found online at https://doi.org/10.1016/j.phro.2023.100517.

References

[1] Via R, Hennings F, Fattori G, Fassi A, Pica A, Lomax A, et al. Non-invasive eye localization in ocular proton therapy through optical eye tracking: a proof of concept. Med Phys 2018;45:2186–214. https://doi.org/10.1002/mp.12841.
[2] Villanueva A, Cabeza R. A novel Gaze Estimation System With One Calibration Point. IEEE Trans Syst Man Cybern 2008;38:1123–38. https://doi.org/10.1109/TSMCB.2008.926606.
[3] Via R, Fassi A, Fattor G, Fontana G, Pella A, Tagaste B, et al. Optical eye tracking system for real-time noninvasive tumor localization in external beam radiotherapy. Med Phys 2015;42:2194–202. https://doi.org/10.1118/1.4915921.
[4] Corbett M, O'Brart D, Stultiens B, Jongsma MF. Corneal Topography using a new Moiré Image-based System. JCRS 1995;7:353–70. https://doi.org/10.1016/S0955-3681(13)80393-0.
[5] Iskander R, Wachel P, Simpson P, Consejo A, Jesus D. Principles of operation, accuracy and precision of an Eye Surface Profiler. OPO 2016;36:266–78. https://doi.org/10.1111/opo.12292.
[6] Jongsma F, De Brabander J, Hendrikse F, Stultiens B. Development of a wide field height eye topographer: validation on models of the anterior eye surface. Optom Vis Sci 1998;75:69–77. https://doi.org/10.1097/00006324-199801000-00027.
[7] EagletEye. Eye Surface Profiler; https://www.eaglet-eye.com; 2023 [accessed 10 November 2023].
[8] Price G, Parkhurst J, Sharrock S, Moore C. Real-time optical measurement of the dynamic body surface for use in guided radiotherapy. Phys Med Biol 2012;57:415–36. https://doi.org/10.1088/0031-9155/57/2/415.
[9] Takeda M, Mutoh K. Fourier transform profilometry for the automatic measurement of 3-D object shapes. Appl Opt 1983;22:3977–82. https://doi.org/10.1364/AO.22.003977.
[10] Takeda M, Ina H, Kobayashi S. Fourier-transform method of fringe-pattern analysis for computer-based topography and interferometry. J Opt Soc Am 1982;72:156–60. https://doi.org/10.1364/JOSA.72.000156.
[11] Takeda M. Measurements of Extreme Physical Phenomena by Fourier Fringe Analysis. AIP Conference Proceeding 2010:1236. doi: 10.1063/1.3426157.
[12] Parkhurst J, Price G, Sharrock P, Moore C. Phase unwrapping algorithm for use in a true optical body sensor system for use during radiotherapy. Appl Opt 2011;50:6430–648. https://doi.org/10.1364/ao.50.006430.
[13] Herràez M, Burton D, Lalor M, Gdeisat M. Fast two-dimensional phase-unwrapping algorithm based on sorting by reliability following a noncontinuous path. Appl Opt 2002;41:7437–44. https://doi.org/10.1364/AO.41.007437.
[14] Ghiglia D, Romero L. Robust two-dimensional weighted and unweighted phase unwrapping that uses fast transforms and iterative methods. J Opt Soc Am 1994;11:107–17. https://doi.org/10.1364/JOSAA.11.000107.

[15] Goldstein R, Zebker H, Werner C. Satellite radar interferometry: Two-dimensional phase unwrapping. Radio Sci 1988;23:713–20. https://doi.org/10.1029/RS023i004p00713.
[16] An Y, Hyun J, Zhang S. Pixel-wise absolute phase unwrapping using geometric constraints of structured light system. Opt Express 2016;24:18445–59. https://doi.org/10.1364/OE.24.018445.
[17] Zuo C, Huang L, Zhang M, Chen Q, Asundi A. Temporal phase unwrapping algorithms for fringe projection profilometry: A comparative review. Opt Lasers Eng 2016;85:84–103. https://doi.org/10.1016/j.optlaseng.2016.04.022.
[18] Vo M, Wang A, Pan B, Pan T. Hyper-accurate flexible calibration technique for fringe-projection-based three-dimensional imaging. Opt Express 2012;20:16926–41. https://doi.org/10.1364/OE.20.016926.
[19] Du H, Wang Z. Three-dimensional shape measurement with an arbitrarily arranged fringe projection profilometry system. Opt Letters 2007;32:2438–40. https://doi.org/10.1364/OL.32.002438.
[20] Feng S, Zuo C, Zhang L, Tao T, Hu Y, Yin W, et al. Calibration of fringe projection profilometry: A comparative review. Opt Lasers Eng 2021;143:e106622.
[21] Takeda M. Fourier Fringe Demodulation. In: Rastogi P,Hack E, editors. Phase Estimation in Optical Interferometry. Taylor&Francis Group. 2014.
[22] Via R, Fattori G, Pica A, Baroni G, Lomax A, Weber D, et al. Eye Tracking in Ocular Proton Therapy. ETRA '20 Adjunct 2020;5:1–3. https://doi.org/10.1145/3379157.3391991.
[23] Hartley R, Zisserman A. Multiple view Geometry in Computer Vision. 2nd ed. Cambridge: University Press; 2006.
[24] Besl PJ, MacKay ND. A method for registration of 3-D shapes. IEEE T Pattern Anal Mach Intell 1992:14239–56. https://doi.org/10.1109/34.121791.
[25] Via R, Hennings F, Pica A, Fattori G, Beer J, Peroni M, et al. Potential and pitfalls of 1.5T MRI imaging for target volume definition in ocular proton therapy. Radiother Oncol 2020:154.53-59. doi: 10.1016/j.radonc.2020.08.023.
[26] Xu J, Zhang S. Status, challenges and future perspective of fringe projection profilometry. Opt Lasers Eng 2020;135:e106193.
[27] Hu Y, Chen Q, Sa F, Zuo C. Microscopic fringe projection profilometry: a review. Opt Lasers Eng 2020;135(e106192). https://doi.org/10.1016/j.optlaseng.2020.106192.
[28] Li B, Zhang S. Superfast high-resolution absolute 3D recovery of a stabilized flapping light process. Opt Express 2017;25:27270–82. https://doi.org/10.1364/OE.25.027270.